Unified Material-Environment Interaction Model for Binary UHTC Composites

N. S. Campbell*, Samuel Y. Chen†, and Iain D. Boyd‡
University of Colorado, Boulder, CO, 80309

Matthew J. Gasch§ and Donald T. Ellerby¶
NASA Ames Research Center, Moffet Field, CA, 94035

A new model for the surface chemistry of zirconium and hafnium diborides containing silicon-carbide when exposed to high temperature conditions in air is formulated. Oxidation dynamics are simplified by considering the diffusion-limited equilibrium regime within the material at elevated temperatures. This model is first assessed against experimental mass-gain data taken from UHTC samples heated to high temperature in an oxygen environment. Then, further evaluations of the new model are conducted using hypersonic CFD simulations to analyze conditions experienced by HfB_2-SiC in arc jet experiments conducted at NASA Ames Research Center. Measurements of stagnation point heat transfer and pressure are then used to calibrate the simulations. Results of coupled CFD-material response simulations are then compared to the surface temperatures measured during the Ames arc jet test. Results support the use of the proposed model while highlighting the need for improved gas-phase data on the additional constituents considered.

Nomenclature

Symbols

a	=	Activity
A	=	Area, m^2
C_M	=	Mass transfer coefficient
D	=	Diffusion coefficient, $m^2\ s^{-1}$
f	=	Volume fraction
G	=	Gibbs free energy, J mol^{-1}
h	=	Height, m
J	=	Species mass flux, kg $m^{-2}\ s^{-1}$
K	=	Equilibrium constant
L	=	Length, m
$\mathcal{M}$	=	Molecular Weight, kg mol^{-1}
$\dot{m}$	=	Mass flux, kg s^{-1}
n	=	Number density, m^{-3}
N	=	Molar site density, moles m^{-2}
N_A	=	Avogadro's Number, 6.02 x 10^{23} mol^{-1}
ϕ	=	Porosity
P	=	Pressure, Pa
R	=	Universal gas constant, 8.314 J $(mol\ K)^{-1}$
t	=	Time, s
τ	=	Tortuosity
T	=	Temperature, K
u	=	Velocity, m s^{-1}
v	=	Molar volume, $cm^3\ mol^{-1}$
Y	=	Mass Fraction
ρ	=	Density, kg m^{-3}
Q	=	Heating Flux, W m^{-2}

Subscripts

g	=	Gas phase
l	=	Liquid phase
s	=	Solid phase
i	=	Species
w	=	Wall/gas-surface interface
e	=	Environment/ambient
diff	=	Diffusive
oxide	=	Oxide layer
liquid	=	Liquid in oxide layer
dep	=	SiC depletion layer

*Post-Doctoral Research Associate, Aerospace Engineering, and AIAA Member
†Post-Doctoral Research Associate, Aerospace Engineering, and AIAA Member
‡H. T. Sears Memorial Professor and National Security Faculty Director, Aerospace Engineering, and AIAA Fellow
§Research Scientist, Entry Systems and Vehicle Development Branch
¶Research Scientist, Thermal Protection Materials Branch

I. Introduction

Ultra-high Temperature Ceramics (UHTCs) are of interest to the scientific community for their elevated melting points and hardness, along with chemical inertness, and oxidation resistance[1, 2]. These resilient characteristics to extreme environments have made UHTCs prime candidates for sharp leading edges and reusable control surfaces of hypersonic vehicles. Unlike ablative Thermal Protection Systems (TPS), structures made from UHTCs are expected to maintain their shape in order to sustain controlled and efficient flight. Understanding the limits of these materials is thus of great importance to the successful operation of future high-speed flight vehicles.

High temperature testing has revealed a complex response of these materials as they transition between passive and active regions of oxidation. Under some test conditions, a temperature-jump phenomenon has been recorded. Results from such tests are shown in Fig. 1. The resulting surface temperature rise in time, during arc jet testing on a sample of HfB_2 with 20% SiC is shown in Fig. 1(a). These tests took place at NASA Ames Rsearch Center and are used later in this study to compare with coupled CFD-material response simulations. Figure 1(b) comes from plasmatron experiments performed at the Von Karmen Institute, on ZrB_2 with 30% SiC and shows how the temperature jump can be attributed to increased chemical heating[3]. This is seen by the surface heat flux jumping from the slightly catalytic ($\gamma = 0.01$) heat flux around 2200 K to nearly fully catalytic ($\gamma \approx 1.0$). While this is suggestive of an explanation for the temperature jump, more work is needed to fully understand and capture the mechanisms leading to this increase in chemical heating at the surface. Past modeling efforts by Chen and Boyd have been able to successfully model

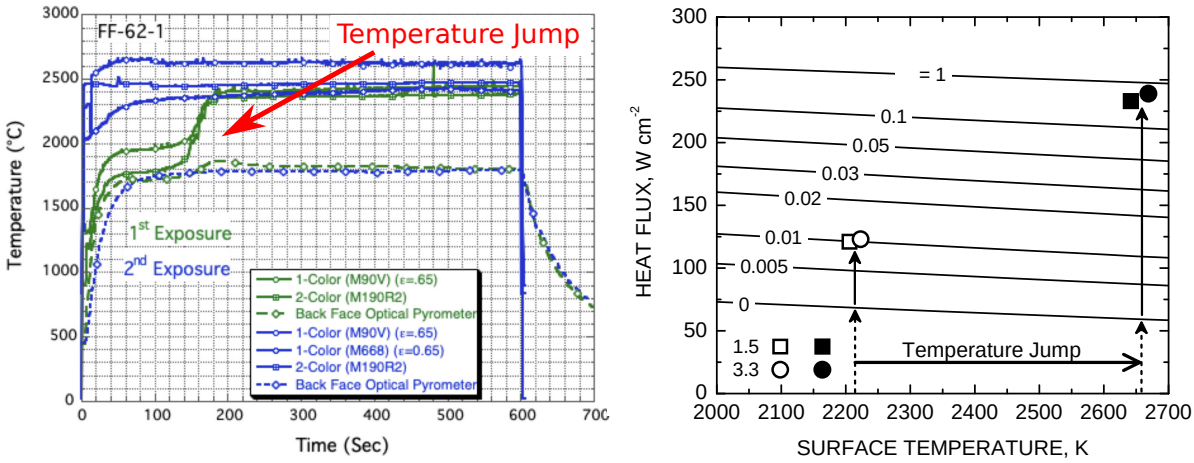

(a) (b)

Figure 1: Examples of experimental studies showing the temperature-jump phenomenon. (a) Results from NASA Ames arc jet testing of HfB_2-20% SiC. (b) Theory and results from plasmatron testing on ZrB_2-30% SiC[3].

the passive-active transition and reproduce a temperature-jump material response of a UHTC sample of SiC[4]. An example result from this work is shown in Fig. 2. Note how the wall temperature jumps 400 K in seconds, correlating to a steep rise in the B' property that is directly related to the total mass flow rate of gas blowing off the surface. To determine these surface fluxes, the 0-D, steady-state equilibrium code, ACE [5], was used[6, 7]. This however only captures surface oxidation which is reasonable for SiC but does not capture internal, in-depth oxidation mechanisms which are important for the ZrB_2/HfB_2 materials. Based on these past experiences, it was concluded that the 0-D ACE approach neglects too many important mechanisms to be useful for ZrB_2/HfB_2, which motivates the need for higher-fidelity model development.

In this work a new model is developed to account for in-depth oxidation processes occurring near the gas-surface interface in binary UHTC composites. Like past modeling efforts, furnace testing results of mass-gain from passive oxidation are used to assess the surface chemistry model while data from NASA Ames arcjet tests are compared with coupled CFD-material response simulations for more complete validation. The main challenge is to relate in-depth micro/meso-scale processes ocurring in a thin layer of the material at the gas-surface interface, to macroscopic processes ocurring on either side, the external flow and internal material. The model needs to provide the gas fluxes exchanged at the surface (both consumption and outgassing), which determines the macroscopic surface mass and energy balance, thus coupling the external flowfield and internal material response.

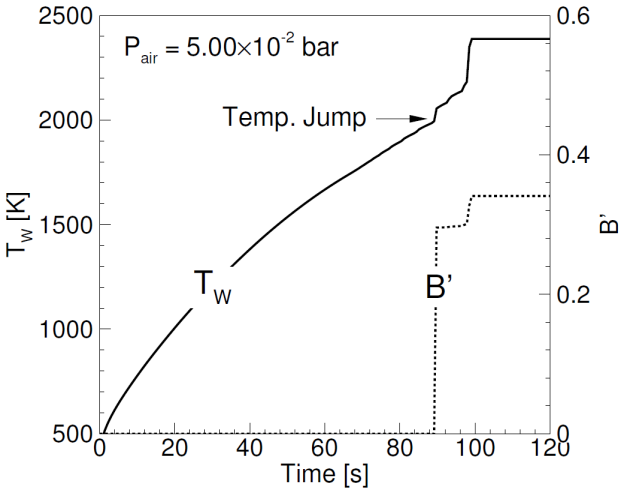

Figure 2: Results from Chen and Boyd showing the temperature jump phenomenon[4]

The following sections cover details and results from two test cases considered. Data is included on the proposed reaction mechanism and extensions are described to apply the model in transient and fluid simulations. First, key aspects of the new model are developed and described.

II. ZrB_2/HfB_2-SiC Surface Chemistry Model

A. Background

The proposed model borrows largely from the work of Parthasarathy [8, 9], but extends it to account for arbitrary gas compositions and materials. Unlike previous modeling attempts, which considered a fully-discretized 1-D transient approach [10], a 1-D *steady-state* approach is considered in this work to model the internal diffusion-limited equilibrium regime. This aims to decouple the diffusion processes from the equilibrium calculations driving the microstructure evolution.

The primary reaction system considered in the current work is described by Reactions (1) to (4) along with the associated mass gain/loss. The generic species, Me, represents either Zr or Hf. In the physical system, there are also numerous secondary reactions that occur. This system is limited by the inward diffusion of oxygen (and corresponding outward diffusion of gaseous oxidation products).

$$\mathrm{MeB_2}(s) + \frac{5}{2}\mathrm{O_2}(g) \rightarrow \mathrm{MeO_2}(s) + \mathrm{B_2O_3}(l) \quad \left[+80.0 \text{ g/mol} \right] \tag{1}$$

$$\mathrm{B_2O_3}(l) \rightarrow \mathrm{B_2O_3}(g) \quad \left[-69.6 \text{ g/mol} \right] \tag{2}$$

$$\mathrm{SiC}(s) + \frac{3}{2}\mathrm{O_2}(g) \rightarrow \mathrm{SiO_2}(l) + \mathrm{CO}(g) \quad \left[+20.0 \text{ g/mol} \right] \tag{3}$$

$$\mathrm{SiC}(s) + \mathrm{O_2}(g) \rightarrow \mathrm{SiO}(g) + \mathrm{CO}(g) \quad \left[-40.1 \text{ g/mol} \right] \tag{4}$$

B. Model Description

Two distinct regions are present in the oxidized material based on the morphology observed in experiments: the oxide layer and the SiC depletion layer. A schematic of the model along with experimental images of the corresponding regions are shown in Fig. 3. SiC depletion occurs internally because it's oxidation is thermodynamically preferred in oxygen-limited environments at temperatures above ~1200 K. The equilibrium behavior of the depletion layer is modeled by reacting a small amount of O_2 with the MeB_2-SiC material in a closed-system calculation, assuming constant temperature and volume, and performed using the multiphase equilibrium solver of Cantera [11]. Thermodynamic data for the various gas, solid, and liquid phases are taken from NASA polynomials [12] and NIST [13]. This calculation relies on the assumption of unit activity for the solid phases, where changes to the chemical activity of gas phases have negligible effect on the chemical activity of the solid phases. This equilibrium calculation describes the ratios

and chemical potentials in the depletion layer oxidation front. However, oxidation kinetics cannot be determined the from equilibrium calculations alone. For that, we need to compute the internal *fluxes* that are consistent with the local equilibrium states.

Liquid oxides (B_2O_3, SiO_2) produced in the depleted layer are assumed to be transported to the oxide layer. In addition, say SiO(g) gas is produced in the depleted layer (via active oxidation, due to the low local oxygen potential), and may diffuse outward into the oxide layer. In the oxide layer, where the oxygen potential is higher, condensed SiO_2(l) may form from SiO(g) recombination, contributing to the overall amount of SiO_2(l) present in equilibrium.

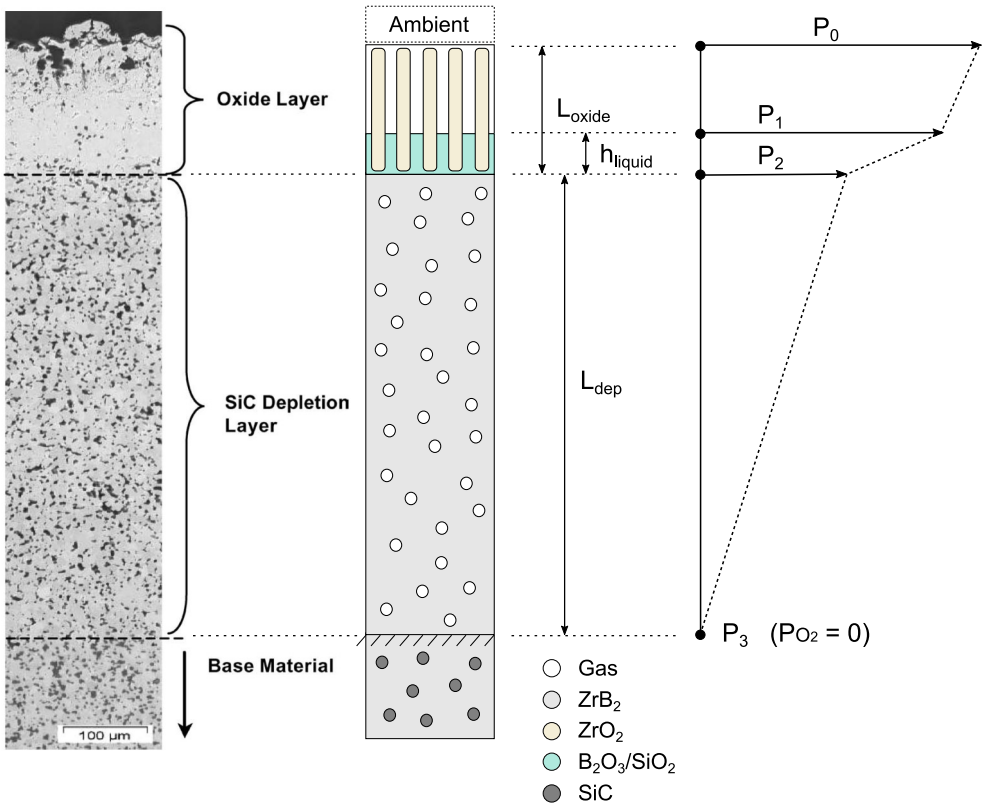

Figure 3: Schematic for 1-D steady-state analysis of ZrB_2/SiC. Experimental micrograph from Gasch et al. [1].

Consider a general isothermal, isobaric system (fixed T, P), with known oxide lengths L_{oxide} and L_{dep} (e.g. measured from experiments). In general, the diffusion flux is given by Fick's law, expressed here in terms of number densities:

$$J_i = -D_i \nabla n_i = -\frac{D_i}{RT} \nabla P_i \tag{5}$$

Diffusion coefficients of gaseous species D_g in the pores are assumed to be equal, based on the Lennard-Jones potentials of O_2, which are well-known [11]. The height of the liquid layer is estimated from the assumed molar site densities (moles/m^2) $N_{B_2O_3}$ and N_{SiO_2}. For a given molar volume ($\nu_{B_2O_3}$ = 27.30 cm^3/mole and ν_{SiO_2} = 27.31 cm^3/mole):

$$h_{\text{liq}} = \frac{N_{B_2O_3} \nu_{B_2O_3} + N_{SiO_2} \nu_{SiO_2}}{\phi_{\text{oxide}}} \tag{6}$$

In general, $h_{\text{liquid}} << L_{\text{oxide}}$, so the diffusion length of the oxide layer is negligibly affected by changes in the liquid layer. The effective diffusion coefficient of O_2 through liquid B_2O_3 is given by Luthra [8, 14]:

$$D_{O_2-B_2O_3} = 1.5 \times 10^{-1} RT \exp\left(\frac{16000\ K}{T}\right) \left[\frac{\text{m}^2}{s}\right] \tag{7}$$

The factor of RT arises from the conversion between permeability (based on a gradient in pressure) and diffusivity (based on a gradient in number density):

$$\nabla P = RT\nabla n \tag{8}$$

Likewise, the effective diffusion coefficient of O_2 through liquid SiO_2 is given by Kajihara [15, 16]:

$$D_{O_2-SiO_2} = 5.9 \times 10^{-9} \exp\left(\frac{-11165\ K}{T}\right) \left[\frac{\mathrm{m}^2}{s}\right] \tag{9}$$

The effective diffusion coefficient through the B_2O_3-SiO_2 liquid mixture is simply the volume-averaged diffusion coefficients of the constituents:

$$f_i \propto N_i v_i \tag{10}$$

$$D_{\mathrm{liq},i} = \frac{f_{B_2O_3} D_{i-B_2O_3} + f_{SiO_2} D_{i-SiO_2}}{f_{B_2O_3} + f_{SiO_2}} \tag{11}$$

The diffusion coefficients of other gases through the liquid are also assumed to be equal. The effective porosity is due to some characteristic porosity for the ZrO_2 or HfO_2 formation ϕ_{MeO_2} and a tortuosity factor τ.

$$\phi_{\mathrm{oxide}} = \frac{\phi_{MeO_2} + f_{SiC}}{\tau} \tag{12}$$

$$\phi_{\mathrm{dep}} = \frac{f_{SiC}}{\tau} \tag{13}$$

ϕ_{MeO_2} is typically on the order of 10^{-2}, and τ is on the order of 10^2 [8]. With this formulation, the steady-state diffusion problem is then given by:

$$J_{0-1,i} = J_{1-2,i} = J_{2-3,i} \tag{14}$$

$$\phi_{\mathrm{oxide}} D_{g,i} \frac{n_{0,i} - n_{1,i}}{L_{\mathrm{oxide}}} = \phi_{\mathrm{oxide}} D_{\mathrm{liq},i} \frac{n_{1,i} - n_{2,i}}{h_{\mathrm{liquid}}} = \phi_{\mathrm{dep}} D_{g,i} \frac{n_{2,i} - n_{3,i}}{L_{\mathrm{dep}}} \tag{15}$$

n_0 and n_3 are known *a priori*, and n_1 and n_2 are the primary unknowns for each specie (2 unique equations, 2 unknowns).

$$n_1 = \frac{(\alpha + \beta) n_0 + n_3}{1 + \alpha + \beta} \tag{16}$$

$$n_2 = \beta(n_0 - n_1) + n_3 \tag{17}$$

However, the height of the liquid layer is not exactly known and thus adds a third unknown. This is related to the number of moles of B_2O_3 and SiO_2 present. The amount of B_2O_3 and SiO_2 is coupled to both equilibrium and diffusion calculations, and thus requires an iterative approach to converge. The equilibrium condition provides the additional relation needed to obtain closure, although it does so implicitly through the equilibrium calculation between the gas composition and condensed phases. This iterative approach solves for the amount of B_2O_3 and SiO_2 that satisfies both steady-state diffusion and equilibrium. For a given h_{liq} (related to the number of moles of B_2O_3 and SiO_2 present in equilibrium), n_1 and n_2 are computed by solving the steady-state diffusion problem, and the value of h_{liq} is iterated upon using a Newton-Raphson scheme.

It should be noted that the internal equilibrium state is only used to evaluate the convergence criterion- the fluxes themselves are determined solely from the ambient and depleted states n_0 and n_3, and the liquid content (both B_2O_3 and SiO_2), strictly satisfying the diffusion constraint. However, the *elemental* composition of the internal gas (n_1 and n_2) will still be in equilibrium with the liquid content when converged, although perhaps in a slightly different molecular configuration. The convergence criteria used is the L_2 norm of the computed fluxes across all gaseous species, where a value of $\varepsilon = 1 \times 10^3\ \mathrm{cm}^{-2}\mathrm{s}^{-1}$ is found to work well:

$$||J^{i+1} - J^i||_2 < \varepsilon \tag{18}$$

Once a converged solution is obtained, the internal diffusion fluxes are solved for. These fluxes provide all the data necessary to evaluate mass loss/gain rates, O_2 consumption, etc. The fluxes exchanged at the surface are of particular interest:

$$\dot{m}_{O_2} = J_{O_2} \frac{\mathcal{M}_{O_2}}{N_A} \quad \left[\frac{\text{kg}}{\text{m}^2 - \text{s}}\right] \tag{19}$$

$$\dot{m}_g = \sum_{i \in \text{out}} J_i \frac{\mathcal{M}_i}{N_A} \quad \left[\frac{\text{kg}}{\text{m}^2 - \text{s}}\right] \tag{20}$$

$$\dot{m}_{\text{net}} = \dot{m}_{O_2} - \dot{m}_g \tag{21}$$

The model may be reduced to evaluate pure ZrB_2/HfB_2 simply by setting both f_{SiC} and L_{dep} to zero (no SiC depletion zone will be present).

1. Transient Modifications

Extending the above steady-state approach to account for transient behavior is relatively simple. Rather than a strict steady-state assumption, a *quasi*-steady state approach is utilized (implicitly assuming that the chemical kinetic timescales are much faster than the diffusion timescales). The oxide and depleted lengths are initialized to a small value ($\sim 10^{-6}$ m), and the system is allowed to evolve time-accurately following the quasi-steady state approach, modeling the growth of various regions due to the computed oxidation kinetics.

Up to now, no assumptions have been made about the dominant reaction mechanisms. Relating the flux of O_2 to the bulk oxidation rate of ZrB_2/HfB_2-SiC is relatively trivial (assumed to be the same). However, relating the bulk oxidation rates to the growth of the oxide and depleted layers depends on the exact reactions that consume the oxygen. For example, Reaction (1) contributes to the growth of the oxide layer (formation of additional MeO_2), while Reactions (3) and (4) contribute to the growth of the depletion layer, and both reaction pathways consume oxygen.

The multiphase equilibrium calculation [11] implicitly accounts for the thermodynamic preference of the two separate reaction pathways in oxygen-limited environments. However, in order to model the growth of the oxide and depleted layers, the dominant reaction mechanism needs to be determined analytically. Assuming that Reactions (1) to (4) occur stoichiometrically, and that the steady-state O_2 flux inward is equal to the total oxidation rate, then the oxidation rate may be split into two separate components:

$$J_{O_2}^{\text{total}} = J_{O_2}^{MeB_2} + J_{O_2}^{\text{SiC}} \tag{22}$$

$J_{\text{SiC}}^{O_2}$ describes the flux of O_2 consumed by SiC oxidation reactions (3) and (4). From these reactions, note that the stoichiometric ratio of SiC to CO is 1:1, which suggests that the number flux of CO *outward* is equal to the rate of SiC oxidation internally. In practice, some CO_2 may be present from the equilibrium calculations, so it is also included in this count. This method is analogous to the "counter-diffusion of CO/CO_2" utilized by Parthasarathy to determine the SiC depletion region [9]. However, both Reactions (3) and (4) may occur in parallel, and the stoichiometric ratio of O_2 to SiC lies between 1.0 and 1.5, depending on which reaction is more dominant at the given temperature and pressure conditions. Equilibrium constants can be determined for each of the assumed SiC reactions, assuming unit activity for the solid/liquid species:

$$\text{SiC}(s) + \frac{3}{2}\text{O}_2(g) \rightarrow \text{SiO}_2(l) + \text{CO}(g), \quad K_3 = \frac{a_{\text{CO}}}{(a_{O_2})^{3/2}} = \exp\left(\frac{-\Delta G_3^0}{RT}\right) \tag{23}$$

$$\text{SiC}(s) + \text{O}_2(g) \rightarrow \text{SiO}(g) + \text{CO}(g), \quad K_4 = \frac{a_{\text{CO}}}{a_{O_2}} = \exp\left(\frac{-\Delta G_4^0}{RT}\right) \tag{24}$$

$$\tag{25}$$

At equilibrium, the activity of CO a_{CO} must be constant, but the *equilibrium activity* of oxygen a_{O_2} is reaction-dependent (since we are considering an oxygen-limited system):

$$a_{O_2}^{R_3} = \left(\frac{a_{\text{CO}}}{K_3}\right)^{2/3} \tag{26}$$

$$a_{O_2}^{R_4} = \frac{a_{\text{CO}}}{K_4} \tag{27}$$

A *lower* equilibrium oxygen activity suggests that the reaction is more dominant in oxygen-limited environments (as $P_{O_2} \to 0$), since less oxygen is required to maintain equilibrium. Assuming that equilibrium oxygen activity is *inversely* related to the weighting yields Eq. (28) for the effective ratio of O_2 to SiC:

$$\frac{N_{O_2}}{N_{SiC}} = \frac{1.5\left(a_{O_2}^{R_3}\right)^{-1} + 1.0\left(a_{O_2}^{R_4}\right)^{-1}}{\left(a_{O_2}^{R_3}\right)^{-1} + \left(a_{O_2}^{R_4}\right)^{-1}} \tag{28}$$

Since the *ratio* of a_{O_2} to a_{CO} is determined by equilibrium, we approximate a_{CO} to be unity and solve for a_{O_2}. Figure 4 plots the effective ratio of O_2 to SiC as a function of temperature. Passive oxidation via Reaction 3 is more dominant below 1500 K, and active oxidation via Reaction 4 is dominant above 1500 K.

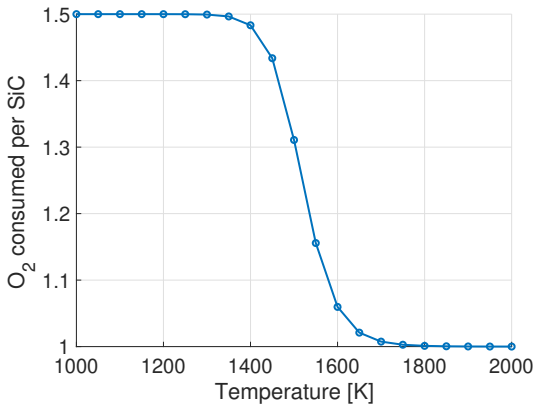

Figure 4: O_2 to SiC ratio.

Based on the above assumptions, this applies only to oxygen-limited environments, such as in the depletion layer, but not at the surface, and corresponds to the effective passive-to-active transition point for SiC in the depletion layer. However, passive oxidation conditions may still be reestablished in the oxide layer at moderate temperatures, due to the higher oxygen potential there. The number flux of O_2 consumed by SiC-related oxidation is then given by:

$$J_{O_2}^{SiC} = (J_{CO} + J_{CO_2})\frac{N_{O_2}}{N_{SiC}} \tag{29}$$

Likewise, the effective "flux" of the SiC constituent oxidized is given by:

$$J_{SiC} = J_{O_2}^{SiC}\frac{N_{SiC}}{N_{O_2}} = (J_{CO} + J_{CO_2}) \tag{30}$$

The number flux of O_2 consumed by ZrB_2 oxidation is then simply the difference between $J_{O_2}^{total}$ and $J_{O_2}^{SiC}$.

$$J_{O_2}^{MeB_2} = J_{O_2}^{total} - J_{O_2}^{SiC} \tag{31}$$

For the MeB_2 reaction, stoichiometrically the ratio of O_2 to MeB_2 is 2.5:1:

$$MeB_2(s) + \frac{5}{2}O_2(g) \to MeO_2(s) + B_2O_3(l) \tag{32}$$

$$J_{MeB_2} = J_{O_2}^{MeB_2}\frac{N_{MeB_2}}{N_{O_2}} = \frac{2}{5}J_{O_2}^{MeB_2} \tag{33}$$

The growth rates of the regions are related to the "fluxes" of SiC and MeO_2 oxidized through the molar volumes ν. For the oxide layer, the volume expansion of MeB_2 to MeO_2 (16.9% for ZrO_2, and 14.1% for HfO_2) is accounted for by

using the molar volume of the oxide:

$$\frac{dL_{\text{oxide}}}{dt} = J_{\text{MeB}_2} \frac{\nu_{\text{MeO}_2}}{1 - f_{\text{SiC}}} \tag{34}$$

$$\frac{dL_{\text{dep}}}{dt} = J_{\text{SiC}} \frac{\nu_{\text{SiC}}}{f_{\text{SiC}}} \tag{35}$$

This approximation is not exact, since additional oxygen atoms may be trapped in species such as CO_2(g) and SiO_2(g) which are not explicitly accounted for in the assumed reaction mechanisms, and do not directly participate in the oxidation reactions. These are generally formed through secondary recombination reactions. However, based on first-order analysis of the unequilibrated fluxes produced, CO is the dominant product, and any CO_2 produced is generally negligible.

$$L_{\text{oxide}}(t + \Delta t) = L_{\text{oxide}}(t) + \frac{dL_{\text{oxide}}}{dt} \Delta t \tag{36}$$

$$L_{\text{dep}}(t + \Delta t) = L_{\text{dep}}(t) + \frac{dL_{\text{dep}}}{dt} \Delta t \tag{37}$$

At very high temperatures (above 3000 K), melting and vaporization of the oxide layer can also occur, but this is currently not accounted for in the model with respect to the oxide layer. Note that the liquid layer does not “grow" with time, as it is enforced to be in multiphase equilibrium with the gas at P_1.

2. Modifications for HfB_2

The analysis may also be extended to HfB_2 if thermodynamic data is employed for Hf-containing species, as oxidation of ZrB_2 and HfB_2 have been shown to be mechanistically similar by other researchers [8, 17]. This model is adapted for HfB_2-based composites by utilizing thermodynamic data for Hf-based species, rather than Zr-based species. Temperature-dependent thermodynamic data for Hf-based species are estimated from their Zr-based counterparts by offsetting the enthalpy (based on the different enthalpies of formation) and entropy. Specifically, data for HfB_2(s), HfO_2(s), HfO_2(g), HfO(g) are estimated from various sources in the literature, and differences in the formation enthalpies and entropies are calculated at $\Delta H_f^0 = -20,040$ J/mol and $\Delta s^0 = +8.99$ J/mol-K, respectively. In addition, HfO_2 has a melting temperature around 100 K higher than ZrO_2 (3050 K vs. 2950 K). Overall, the differences in the predicted volatilities are small, but the higher density of HfO_2 results in increased mass loss rates in the melting temperature regime (above 3000 K).

C. Model Assessment

Figures 5 and 6 are the key results of this analysis, informing detailed CFD and material response simulations. Results are shown in Fig. 5, comparing the temperature-dependent transient mass gain rates. These measurements were taking by Tripp and Graham in the early 1970’s, using a thermogravimetric system specifically designed to measure total oxygen consumption for materials that form a volatile oxide. For a single run, the samples were heated to a constant temperature then exposed to oxygen at this constant temperature while the mass changes of the sample and condensed volatalized oxides on the surrounding crucible were measured in time. It was ensured that enough oxygen was reaching the sample that oxidation rates were note affected by the flow rate. The parabolic mass gain rates are recovered across the range of temperature conditions examined (1000 K to 1700 K), and temperature-dependent oxidation rates are largely consistent with experimental data.

Figure 6 shows the gaseous diffusion fluxes exchanged at the material-environment interface as the result of internal oxidation mechanisms. These fluxes describe the primary material-environment interaction for both ZrB_2 and ZrB_2-SiC materials. For ZrB_2 in Fig. 6(a), B_2O_3 gas is produced via evaporation of liquid B_2O_3. In the gas phase, equilibrium calculations predict that B_2O_3 quickly dissociates into other B-containing species. For ZrB_2-SiC in Fig. 6(b), the kink at 1600 K is due to internal passive-to-active transition in the SiC-depletion layer (see Fig. 4). The gaseous products suggest that SiC oxidation is strongly preferred over ZrB_2 in oxygen-limited environments, which is consistent with the analysis of other researchers [17, 19]. Nonetheless, some ZrB_2 oxidation does occur in parallel, as evidenced from the production of BO gas. The temperature-dependent mass change behaviors of these materials are plotted in Fig. 7. For ZrB_2, the mass gain rate below 2000 K increases with temperature primarily due to the higher gas diffusion coefficient through the liquid B_2O_3 layer, forming both liquid B_2O_3 and solid ZrO_2. Above 2000 K, all liquid B_2O_3 produced is immediately evaporated, and the weight gain is attributed only to formation of solid ZrO_2. Note that assumed oxide lengths do not affect the temperature dependency, only the magnitude of the mass change.

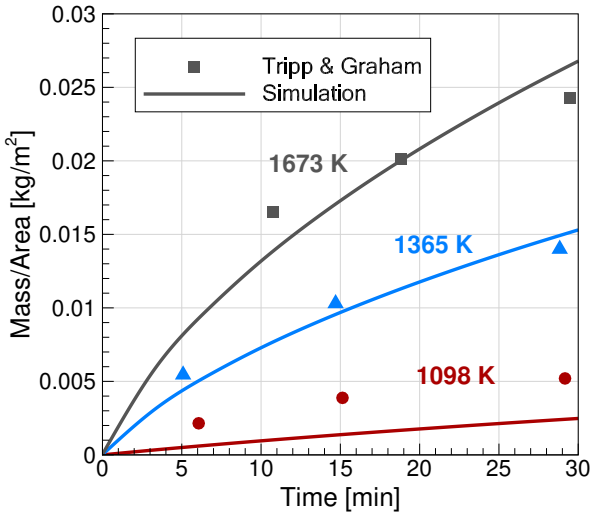

Figure 5: Comparison of ZrB_2 weight change predictions to experimental data of Tripp and Graham [18]. Ambient conditions are 33.3 kPa O_2.

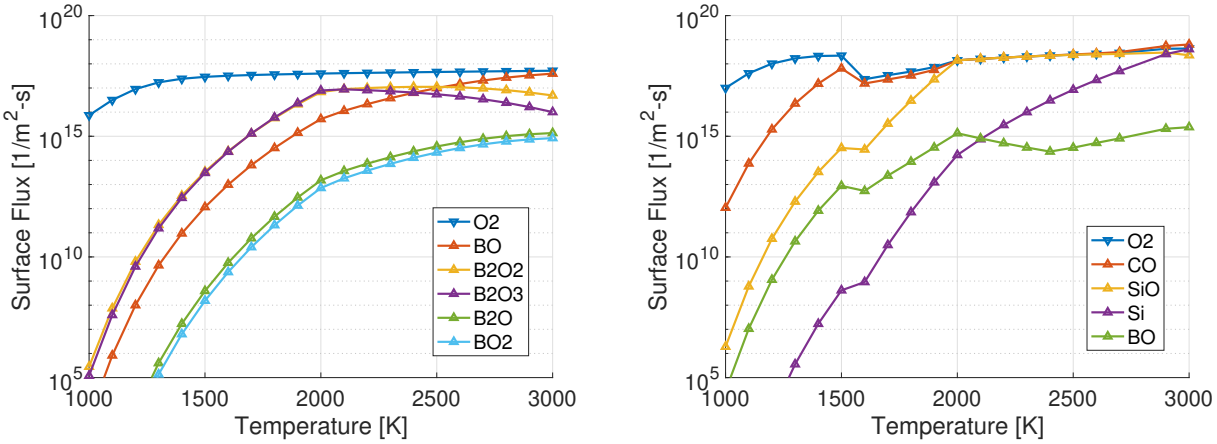

(a) ZrB_2 (b) ZrB_2 w/ 20 vol% SiC

Figure 6: Quasi-steady state fluxes computed over typical oxide lengths measured in experiments (~1 mm) in 1 atm air. "∇" symbol denotes inward flux, and "Δ" denotes outward flux.

The mass change behavior of the composite material is not as straightforward. Below 1500 K, weight gain is primarily attributed to a combination of condensed B_2O_3 and SiO_2 formation (predominantly SiO_2 though, based on the flux of CO). From 1500 K to 2000 K, the depletion layer switches from passive to active oxidation. Passive oxidation conditions are reattained in the porous oxide layer, limiting both the oxidation rate and the mass gain rate. Above 2000 K, SiC oxidation is active throughout, resulting in rapid mass loss that accelerates with increasing temperatures, since both B_2O_3 and SiO_2 phases are volatilized. Figure 8 demonstrates the very high temperature behavior of ZrB_2, including melting and dissociative vaporization of ZrO_2 above 3000 K, where ZrO gas is produced, rather than ZrO_2 gas. This leads to rapid mass loss due to combined vaporization of ZrO_2 and oxidation of ZrB_2.

D. Limitations

The new model demonstrates a marked improvement compared to previous ZrB_2-SiC models[10], and provides a simplified, consistent approach valid across the entire temperature range from 500 K up to 4000 K. A limitation of

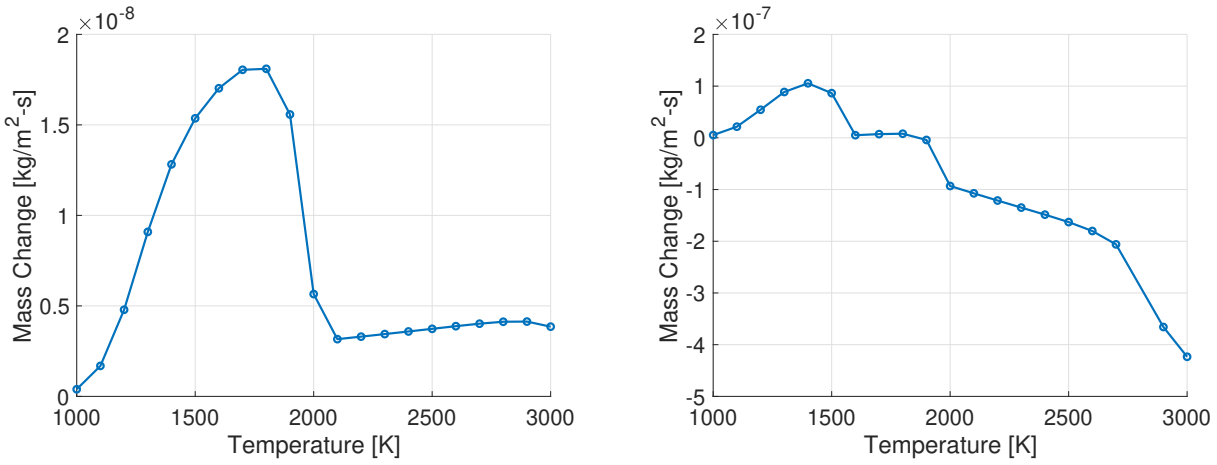

(a) ZrB_2 (b) ZrB_2 w/ 20 vol% SiC

Figure 7: Quasi-steady state, temperature-dependent mass change behavior over typical oxide lengths measured in experiments (~1 mm) in 1 atm air.

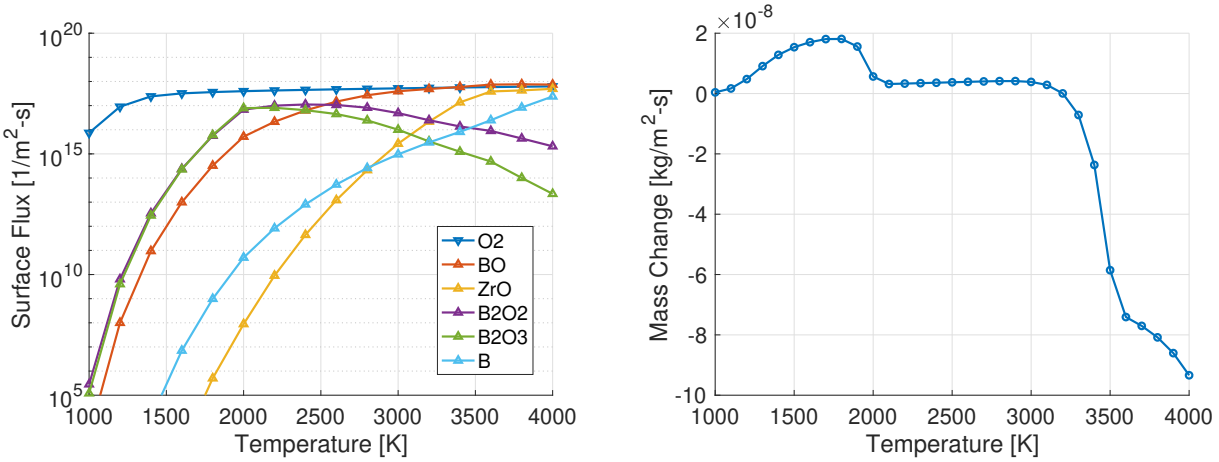

(a) Gas exchange (b) Mass Change

Figure 8: High temperature behavior for ZrB_2 over typical oxide lengths measured in experiments (~1 mm) in 1 atm air.

the steady-state (or quasi-steady state) is that important oxidation processes may in fact occur in the transient, such as the initial growth of the porous region due to ZrB_2 oxidation, even at conditions where SiC oxidation is preferred in steady-state. There are still some discrepancies for bulk ZrB_2-SiC mass change data compared to available experimental measurements [20]. However, there is not a consistent gain/loss trend in the experimental data itself [20], nor are the ambient conditions particularly well characterized. It is also possible that these differences may be attributed to non-equilibrium chemistry, particularly in the internal oxygen-limited conditions.

The model results shown above are tuned to diffusion-limited data (porosities, mixture transport properties). Researchers have shown that the diffusion-limited conditions are not representative of highly convective environments (e.g. arcjets) [9]. Thus, the transient approach as described above is expected to greatly underpredict the physical dimensions of the oxide and depleted layers (and hence the magnitude of the fluxes) in highly convective environments.

Physically, convective environments are expected to mitigate the limiting effects of diffusion on the oxidation kinetics, increasing the effective transport of reactants and products. By parameterizing the equilibrium results into the B' formulation (described below), the effect of increased incident and convective fluxes can be approximated. The proposed approach to model highly convective environments is to assume that the *ratios* given by the diffusion-limited analysis (the B' values) are *independent* of the actual flow conditions, so a higher incident flux simply accelerates the oxidation

rate over the baseline diffusion-limited case (since there is more oxygen reaching the surface). It is hypothesized that the *normalized* fluxes should remain reasonably constant (only a function of T, P), provided that the system remains diffusion-limited (all oxygen is consumed), rather than reaction-limited (not all oxygen is consumed). This assumption needs to be verified, however.

III. CFD and Material Response Integration

The current work uses the finite volume CFD code, LeMANS, to model the hypersonic flow in the arc jet and is capable of capturing thermal and chemical nonequilibrium. The code has been verified against theory and validated against laboratory and flight data[21]. Additionally, the material response code, MOPAR is applied to incorporate the external flow field and gas-surface interface model to determine the bulk material thermal response. The following discussion provides details on the current formulation used to achieve this coupling.

A. B' Table Construction

The diffusion flux (in terms of mass, not number density) of species i at the surface may be defined in terms of mass transfer coefficients:

$$\dot{m}_{\text{diff},i} = -\rho_w D_i \nabla Y_{w,i} = \rho_e u_e C_M (Y_{e,i} - Y_{w,i}) \tag{38}$$

The steady-state mass balance at the gas-surface interface ("w") for species i is given by:

$$\dot{m}_w Y_{w,i} - \dot{m}_{\text{diff},i} = \dot{m}_g Y_{g,i} \tag{39}$$

$$\sum_i \dot{m}_{\text{diff},i} = 0 \tag{40}$$

$$\dot{m}_w = \dot{m}_g \tag{41}$$

Note that this is essentially the same calculation that LeMANS performs with the blowing fluxes [22]. The B' parameter is then defined as:

$$B' = \frac{\dot{m}_g}{\rho_e u_e C_M} = \frac{\dot{m}_w}{\rho_e u_e C_M} \tag{42}$$

$\dot{m}_g$ is easily obtained by summing over the outgoing fluxes in Eq. (20). However, the effective wall enthalpy needs to account for the *mixing* between the ambient ("e") and the blowing gas ("g") given by Fig. 6. Assuming equal diffusion coefficients, the individual species mass fractions of the mixture are given by [5]:

$$Y_{w,i} = \frac{Y_{e,i} + B' Y_{g,i}}{1 + B'} \tag{43}$$

Strictly, the mass transfer coefficient needed to compute the B' values is given by:

$$\left(\rho_e u_e C_M\right)_{\text{diff}} = \frac{\dot{m}_{O_2}}{Y_{e,O_2} - Y_{w,O_2}} \tag{44}$$

$\dot{m}_{O_2}$, $\dot{m}_g$, Y_e, and Y_g are known quantities for the baseline case. This calculation for Y_w, B', and $\rho_e u_e C_M$ is not so straightforward though, since Y_w itself depends on B' (which in turn depends on $\rho_e u_e C_M$). For example, consider a constant flow condition (fixed $\rho_e u_e C_M$, Y_e). Small B' values at low temperatures suggest that $Y_w \approx Y_e$ (not much blowing, although there is still a finite-rate of O_2 consumption). The resulting value of $\rho_e u_e C_M$ will be unphysically large (dividing by near zero), if the assumption is enforced that only the diffusion flux of O_2 is consumed, based on Eq. (44). From Eq. (19), $\dot{m}_{O_2}$ is the flux consumed internally, and relating it to the mass transfer coefficient assumes that *only* the transported O_2 is consumed (and not necessarily that $Y_{w,O_2} = 0$). The quantity $\rho_e u_e C_M$ includes the effect of inert species, so for the baseline diffusion-limited case, an estimate of the *minimum* bulk flux required to sustain steady-state oxidation is obtained by approximating $Y_{w,O_2} = 0$:

$$\left(\rho_e u_e C_M\right)_{\text{min}} = \frac{\dot{m}_{O_2}}{Y_{e,O_2}} \tag{45}$$

This approximation facilitates the calculation of both B' and Y_w, and allows normalized B' tables to be constructed solely from the known quantities (assuming all O_2 at the surface may be consumed if needed, not just the transported O_2). Sample B' plots are shown in Fig. 9 for both HfB_2 and HfB_2-SiC materials, describing the bulk mass fluxes blowing from the surface as a function of temperature. The effects of surface chemistry on the energy balance are captured by the mixture wall enthalpy parameter, h_w.

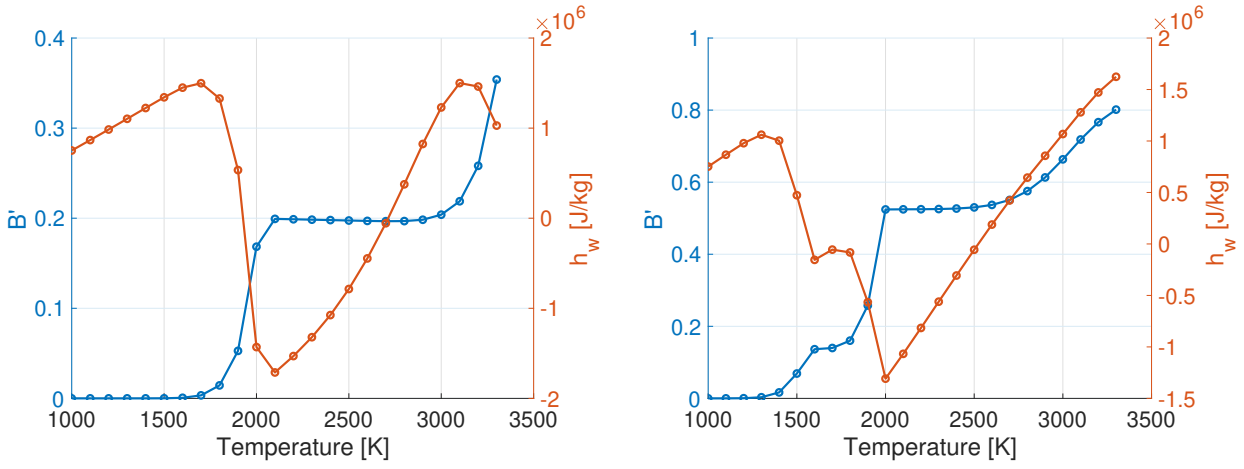

(a) HfB_2 (b) HfB_2 w/ 20 vol% SiC

Figure 9: Sample B' plots in 1 atm air.

Accompanying the B' plots are the equilibrium surface gas compositions in Fig. 10 (used to compute the mixture wall enthalpy h_w). This analysis suggests that oxygen is never fully consumed at the surface. Note that the equilibrium calculation at the surface is modified to include atomic oxygen, but not internally (assumes atomic O behaves similarly to O_2). In equilibrium, atomic oxygen is only relevant for temperatures above 3000 K. There is also a difference between the equilibrated and nonequilibrated mixed gas compositions. Depending on the application, it may be more appropriate to utilize the nonequilibrium blowing fluxes themselves (depends on if the mass and energy contributions are accounted for at the material surface, or in the gas-phase). At the surface, gaseous species such as SiO, CO, HfO tend to recombine into their di-oxygen counterparts (SiO_2, CO_2, HfO_2) due to the higher oxygen potential available at the surface, assuming equilibrium.

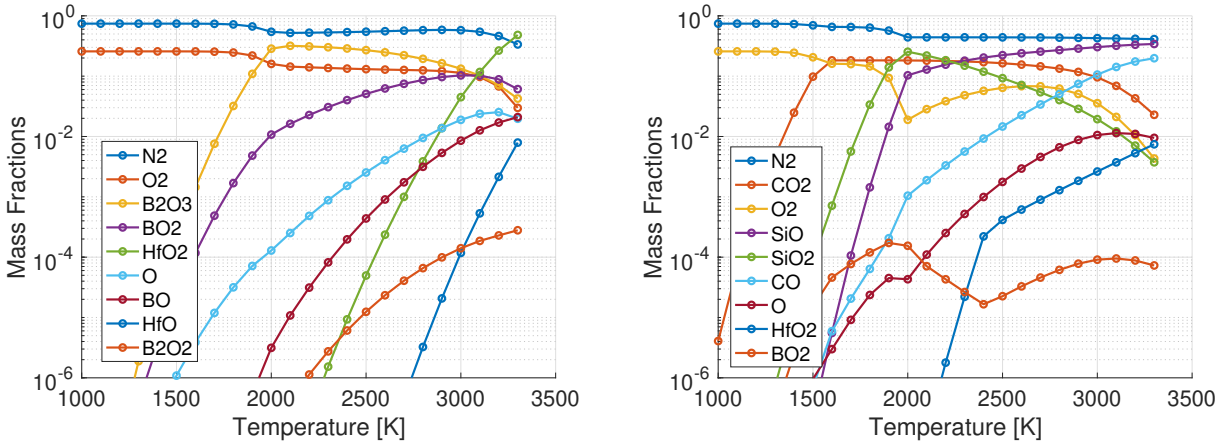

(a) HfB_2 (b) HfB_2 w/ 20 vol% SiC

Figure 10: Equilibrium surface gas compositions in 1 atm air.

B. Limitations

An additional limitation of this B' approach is that the mass *gain* due to formation of condensed oxides is not accounted for, only the gaseous fluxes exchanged at the surface. However, this can be tracked separately (using Fig. 7,

but accounting for variable pressure), assuming the quantity $\rho_e u_e C_M$ remains constant. The ratio of:

$$\Gamma = \frac{\rho_e u_e C_M Y_{e,O_2}}{\dot{m}_{O_2}} \tag{46}$$

should provide the effective “acceleration" factor over the baseline diffusion-limited analysis, including the rates of mass change (scaling linearly), where $\rho_e u_e C_M$ is evaluated independently, i.e. through CFD analysis, or from experimental measurements:

$$\rho_e u_e C_H = \frac{Q_w}{h_r - h_w} \tag{47}$$

$$Le = \frac{C_H}{C_M} \approx 1 \tag{48}$$

Assuming a constant Lewis number and relating C_H to C_M is generally a good assumption, provided that the heat flux is dominated by the diffusive component, e.g. for catalytic surfaces.

IV. Results and Discussion

First, CFD simulations are presented which target and characterize the test condition of interest. Then the new surface chemistry model is applied in material response simulations using the aerothermodynamic heating calculated in LeMANS.

A. Targeting Arc Jet Conditions

Table 1 provides the freestream chemical composition used in this study. These were selected based on the stagnation point measurements of a hemispherical probe with a cold, fully-catalytic wall. These are the conditions for which the temperature jump shown Fig. 1(a) was measured. Inlet conditions are varied to find the chosen settings provided in Tables 1 and 2, which represent the closest match to experimentally measured values. Freestream species concentrations are set assuming thermal and chemical equilibrium. The open-source chemistry solver Cantera is used to solve for mixture densities at specified inlet conditions[11]. The resulting flowfield details of the selected hemisphere case is shown in Fig. 11.

Table 1: Arc Jet Test Conditions

Mach Number	h_{tot} **[MJkg^{-1}]**	ρ **[kg m^{-3}]**	**T [K]**	**V [km s^{-1}]**
6.8	24.2	2.12 x 10^{-4}	2362	6.25

Table 2: Freestream Constituents

X_{N2}	X_{O2}	X_{NO}	X_N	X_O	X_{N2+}	X_{O2+}	X_{NO+}	X_{N+}	X_{O+}	X_{e-}
0.753	0.158	0.015	1.70 x 10^{-6}	0.07	0.0	1.29 x 10^{-13}	2.49 x 10^{-9}	0.0	0.0	2.49 x 10^{-9}

Figure 11(a) shows contours of Mach number which provides a clear shock and Fig. 11(b) provides the gas temperature variation. After measuring the arc jet conditions using the hemispherical probe, a sample of HfB_2 with 20% SiC shaped as a flat-faced coupon was positioned into the high-temperature jet. Thus, the target conditions chosen from the hemispherical probe simulations are applied to a flat-face coupon. The resulting flowfield around this material sample is shown in Fig. 12.

The flowfields and resulting surface loads on the material sample are much different than for the hemispherical probe. The stagnation line properties are compared in Fig.13. Relative to the size of the object, the flat-face coupon generates a much thicker shock with greater relative stand-off distance. This increased stand-off distance results in a larger reservoir of compressed, high-temperature gas that must expand around the coupon’s shoulder. This increases the shear stress and subsequently the convective heating to the surface.

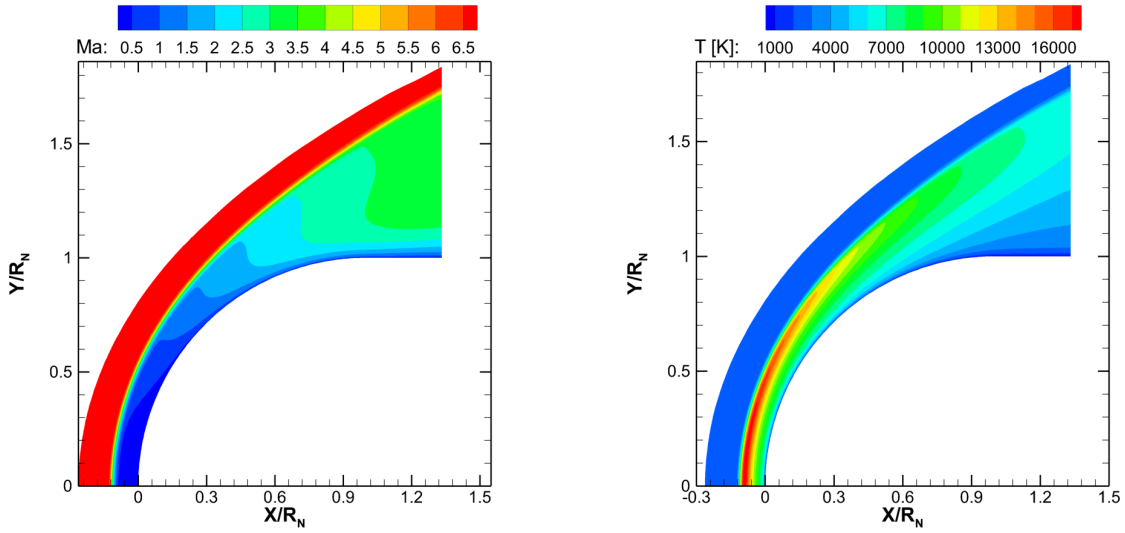

Figure 11: Calibration case using a hemisphere with a cold, fully-catalytic wall.

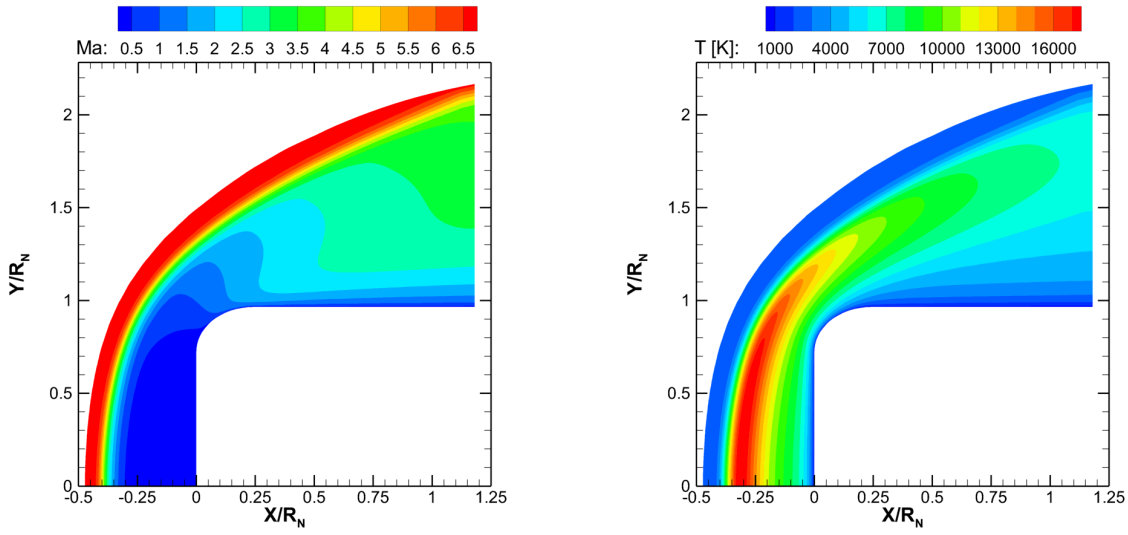

Figure 12: Test case using a flat faced coupon with a cold, fully-catalytic wall.

The resulting surface loads for these two bodies are shown in Fig.14. Arbitrary units are used as this data is ITAR restricted. For the hemisphere, the peak heating and pressure are located near the stagnation line. The coupon however, with it's strong shear flow around the shoulder, experiences peak heating near the outer radius of the front face. For both geometries, excellent agreement is shown with the measured stagnation pressures.

B. Transient Material Response

Using the flow conditions targeted in the previous section, wall pressures and heat fluxes are used as the aerothermodynamic boundary condition in MOPAR. For this study, feedback coupling to the fluid field is not incorporated but will be performed in future work. Temperature dependant thermophysical properties of the HfB_2-SiC are used. B'-tables similar to those shown in Fig. 9 are calculated at various pressures and referenced during the transient simulations.

An example of the axisymmetric solid mesh and snapshots from one of the transient simulations are shown in Fig. 15. Note how the surface deforms and recedes as material is removed over time. With the shoulder experiencing peak heat flux, it wears down faster then the other material. This geometry modification will lead to a change in the surface pressure and heating. However, Fig. 15 only shows a small amount of shape change thus error from maintaining

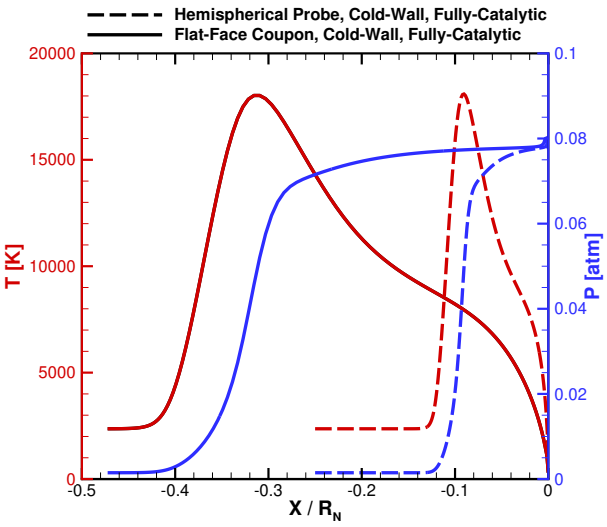

Figure 13: Comparison of stagnation line properties for equivalent flow conditions, over the two geometries of interest.

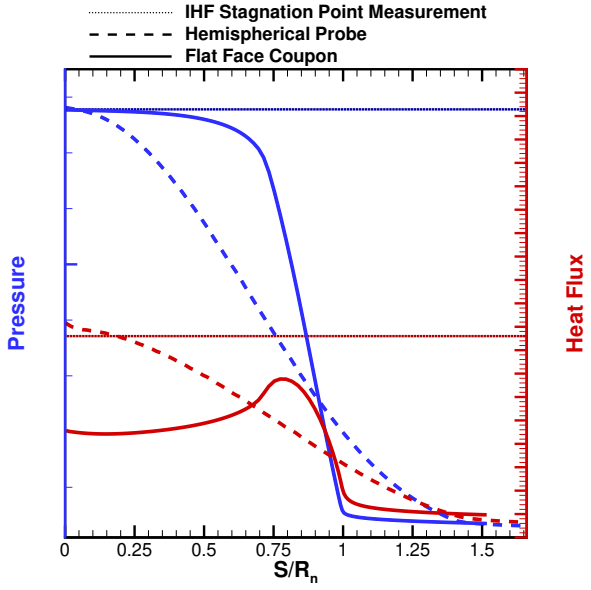

Figure 14: Comparison of aerodynamic surface loads, over the two geometries of interest.

external flow conditions from the steady-state simulations is expected to be small. This run considers a back face held at T_{back} = 1800 K while the other non-symmetry boundaries experience the hypersonic flowfield. The specific boundary conditions on the backside of the sample are not known, so various simulations are performed. First, a 1-D case is run using the targeted stagnation point conditions. This is shown in Fig. 16(a) as the dotted curve which reaches the highest surface temperature. Horizontal lines provide a representative value for the front face and back face measurements shown in Fig. 1(a). It is expected that the 1-D solution provides an overestimate. The actual sample experiences a distribution of heat flux and pressure, along with the multidimensional relaxation from internal conduction.

Finally, multiple cases are run using the axisymmetric distributions of heat flux and pressure from the CFD results. Point results are plotted in Fig. 16(a) from the front face of the maximum surface temperatures. The solid curve shows

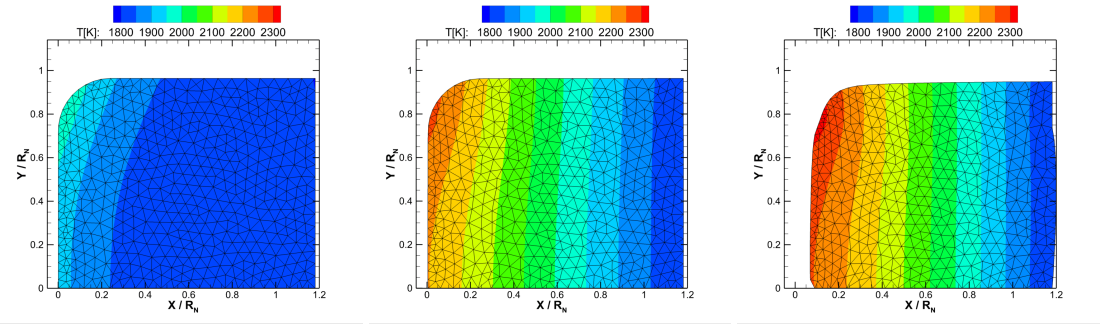

Figure 15: Thermal response of a HfB2-SiC material sample subjected to the surface loads shown in Fig 14. Left to right, these show snapshots from 1s, 10s, and 180s, respectively.

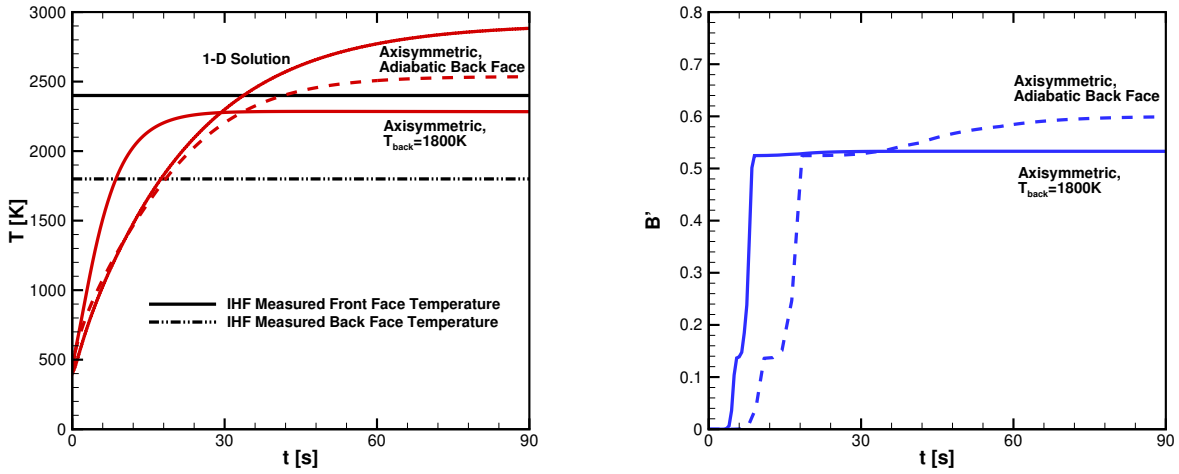

(a) Surface Temperature

(b) Blowing Parameter

Figure 16: Thermal response of a HfB2-SiC material sample subjected to the surface loads shown in Fig 14.

the front face temperature with the back face temperature held at 1800 K. This represents a wall with approximately 40 W cm^{-2} heat leak into the fixture. The resulting simulated steady-state temperature lies just under the experimental value. Note that this result falls at the bottom of the spread of measured temperatures shown in Fig. 1(a). Conversely, the dashed curve shows results from a material sample with an insulated (adiabatic) back face. This results in a predicted steady-state temperature slightly higher than the measurement, while aligning with the upper-end of the spread of values between the different pyrometers.

Figure 16(b) show B' values calculated during the axisymmetric simulations. It is interesting to note the jump-behavior in these cures after the material temperature reaches $\approx$ 1000 K for the fixed back face temperature case. For the adiabatic wall case, B'-jumps are seen after $\approx$ 1500 K and to a lesser extent, after $\approx$ 2400 K. However, the level of blowing is not enough to have a significant effect on the surface energy balance as similar jump-trends are not seen in the temperature.

These results may suggest that the coupling between the surface blowing and the aerothermodynamic loads plays an important role in creating the temperature jump measured in the Ames arc jet facility. More work is needed at incorporating these details into the CFD framework. Overall the new surface chemistry model, using realistic flowfield conditions, is able to recreate the measured steady state temperatures.

V. Conclusion

A new model has been presented that is able to accurately account for the equilibrium surface chemistry of UHTC materials at high temperatures. Assuming the surface material to be in a diffusion limited regime at steady-state allows

for a simple and effective model for handling the complexity of oxidizing zirconium and hafnium diborides containing silicon-carbide. This was assessed and validated against multiple experimental measurements.

While the model is derived as a system at steady-state, it was shown to accurately reproduce mass gain data when compared to thermogravimetric measurements. Discrepancies between predicted and measured values are attributed to a number of potential sources of error including unknown test conditions as well as unmodeled finite-rate chemistry. Future work is needed to understand regimes where nonequilibrium effects may be important and further comparisons with different experimental measurements are warranted.

Measurement taken in NASA Ames arc jet facility provided a test case for the model in a highly convective environment. Arc jet conditions were matched with simulated flow fields and incorporated into material response simulations. Without considering the feedback from the material decomposition to the external flow, surface temperatures were calculated that accurately represent the steady-state temperatures measured. This work provides the foundation for future steps towards better understanding the complex dynamics that lead to temperature jump behavior in binary UHTC composites and provides a useful tool in the process of realizing the promise of UHTCs for thermal protection of hypersonic vehicles.

Acknowledgments

The authors acknowledge support through funding from the U.S. Office of Naval Research, Grant N00014-18-1-2531.

References

[1] Gasch, M., Ellerby, D., Irby, E., Beckman, S., Gusman, M., and Johnson, S., "Processing, properties and arc jet oxidation of hafnium diboride/silicon carbide ultra high temperature ceramics," *Journal of Materials Science*, Vol. 39, No. 19, 2007, pp. 5925–5937.

[2] Gasch, M. and Johnson, S., "Physical characterization and arcjet oxidation of hafnium-based ultra high temperature ceramics fabricated by hot pressing and field-assisted sintering," *Journal of the European Ceramic Society*, Vol. 30, No. 11, 2010, pp. 2337–2344.

[3] Marschall, J., Pejakovic, D. A., Fahrenholtz, W. G., Hilmas, G. E., Zhu, S., Ridge, J., Fletcher, D. G., Asma, C. O., and Thoemel, J., "Oxidation of ZrB_2-SiC Ultrahigh-Temperature Ceramic Composites in Dissociated Air," *Journal of Thermophysics and Heat Transfer*, Vol. 23, No. 2, 2009, pp. 267–278.

[4] Chen, S. Y., Boyd, I. D., Martin, N. C., and Fletcher, D. G., "Modeling of Emission Spectra in Nonequilibrium Plasmas for Testing Pyrolyzing Ablators," *Journal of Thermophysics and Heat Transfer*, Vol. 33, No. 4, 2019, pp. 907–916.

[5] Powars, C. A. and Kendall, R. M., *Aerotherm Chemical Equilibrium (ACE) Computer Program*, User Manual, Aerotherm Corporation, Mountain View, CA, 1969.

[6] Chen, S. Y. and Boyd, I. D., "Chemical equilibrium analysis of silicon carbide oxidation in oxygen and air," *Journal of the American Ceramic Society*, Vol. 102, 2019, pp. 4272–4284.

[7] Chen, S. Y. and Boyd, I. D., "Boundary-Layer Thermochemical Analysis During Passive and Active Oxidation of Silicon Carbide," *Journal of Thermophysics and Heat Transfer*, 2020, pp. 1–12.

[8] Parthasarathy, T. A., Rapp, R. A., Opeka, M., and Kerans, R. J., "A model for the oxidation of ZrB_2, HfB_2 and TiB_2," *Acta Materialia*, Vol. 55, No. 17, 2007, pp. 5999–6010.

[9] Parthasarathy, T. A., Rapp, R. A., Opeka, M., and Cinibulk, M. K., "Modeling oxidation kinetics of SiC-containing refractory diborides," *Journal of the American Ceramic Society*, Vol. 95, No. 1, 2012, pp. 338–349.

[10] Chen, S. Y. and Boyd, I. D., "A thermodynamic meso-scale model for oxidation of ZrB_2-SiC," AIAA Paper 2020-0399, 2020.

[11] Goodwin, D. G., Speth, R. L., Moffat, H. K., and Weber, B. W., "Cantera: An Object-oriented Software Toolkit for Chemical Kinetics, Thermodynamics, and Transport Processes," https://www.cantera.org, 2018, Version 2.4.0.

[12] McBride, B. J., Zehe, M. J., and Gordon, S., *NASA Glenn Coefficients for Calculating Thermodynamic Properties of Individual Species*, NASA TP-2002-211556, NASA Glenn Research Center, Cleveland, Ohio, 2002.

[13] NIST, "NIST Chemistry WebBook," 2020, `https://webbook.nist.gov/`, Last accessed on 2020-01-21.

[14] Luthra, K. L., "Oxidation of carbon/carbon composites—a theoretical analysis," *Carbon*, Vol. 26, No. 2, 1988, pp. 217–224.

[15] Kajihara, K., Kamioka, H., Hirano, M., Miura, T., Skuja, L., and Hosono, H., "Interstitial oxygen molecules in amorphous Si O 2. III. Measurements of dissolution kinetics, diffusion coefficient, and solubility by infrared photoluminescence," *Journal of applied physics*, Vol. 98, No. 1, 2005, pp. 013529.

[16] Raj, R., "Chemical Potential-Based Analysis for the Oxidation Kinetics of Si and SiC Single Crystals," *Journal of the American Ceramic Society*, Vol. 96, No. 9, 2013, pp. 2926–2934.

[17] Poerschke, D. L., Novak, M. D., Abdul-Jabbar, N., Krämer, S., and Levi, C. G., "Selective active oxidation in hafnium boride-silicon carbide composites above 2000 °C," *Journal of the European Ceramic Society*, Vol. 36, No. 15, 2016, pp. 3697–3707.

[18] Tripp, W. C. and Graham, H. C., "Thermogravimetric Study of the Oxidation of ZrB_2 in the Temperature Range of 800 to 1500 C," *Journal of the Electrochemical Society*, Vol. 118, No. 7, 1971, pp. 1195–1199.

[19] Fahrenholtz, W. G., "Thermodynamic analysis of ZrB_2–SiC oxidation: formation of a SiC-depleted region," *Journal of the American Ceramic Society*, Vol. 90, No. 1, 2007, pp. 143–148.

[20] Levine, S. R., Opila, E. J., Halbig, M. C., Kiser, J. D., Singh, M., and Salem, J. A., "Evaluation of Ultra-High Temperature Ceramics for Aeropropulsion Use," *Journal of the European Ceramic Society*, Vol. 22, 2002, pp. 2757–2767.

[21] Scalabrin, L. C., *Numerical Simulation of Weakly Ionized Hypersonic Flow Over Reentry Capsules*, Ph.D. thesis, University of Michigan, Ann Arbor, MI, 2007.

[22] Martin, A. and Boyd, I. D., "Simulation of Pyrolysis Gas Within a Thermal Protection System," AIAA Paper 2008-3805, 2008.